Digital light processing of ceria-stabilized zirconia: Role of powder pre-treatment on printability and physico-mechanical properties

Original
Digital light processing of ceria-stabilized zirconia: Role of powder pre-treatment on printability and physico-mechanical properties / Coppola, B., Fiume, E., Terranova, V., Montanaro, L., Palmero, P.. - In: JOURNAL OF THE EUROPEAN CERAMIC SOCIETY. - ISSN 0955-2219. - ELETTRONICO. - 45:13(2025). [10.1016/j.jeurceramsoc.2025.117512]

Publisher:
Elsevier

Published
DOI:10.1016/j.jeurceramsoc.2025.117512

Journal of the European Ceramic Society 45 (2025) 117512

Contents lists available at ScienceDirect

Journal of the European Ceramic Society

journal homepage: www.elsevier.com/locate/jeurceramsoc

Digital light processing of ceria-stabilized zirconia: Role of powder pre-treatment on printability and physico-mechanical properties

Bartolomeo Coppola *, Elisa Fiume, Vanessa Terranova, Laura Montanaro, Paola Palmero

Politecnico di Torino, Department of Applied Science and Technology, INSTM R.U. Lince Laboratory, Corso Duca Degli Abruzzi, 24, Italy

ARTICLE INFO

Keywords:
Digital light processing
Ceria-stabilized zirconia
Particle size
Microstructure
Flexural strength

ABSTRACT

In this study, the role of pre-treatment of a ceria-stabilized zirconia powder on slurry printability in Digital Light Processing as well as on density, microstructural features and flexural strength of the sintered materials was investigated. Three powder batches, namely un-milled, ball-milled, and ball-milled and thermally post-treated were compared. Ball-milling induced tetragonal-to-monoclinic phase transformation and the appearance of oxygen vacancies. The thermal post-treatment was effective in restoring a higher tetragonal phase content and the starting cerium oxidation state. Slurries with a fixed solid loading (41 vol%) and variable amounts of dispersant were prepared. Different curing behaviors and, consequently, different qualities of the printed parts were observed. The milled and thermally treated powder was used to produce high-density sintered materials characterized by submicrometric grains (≅ 600 nm) and high flexural strength (≅ 560 MPa).

1. Introduction

Among technical oxide ceramics, zirconia stands out for its exceptional combination of structural and functional properties [1], enabling its widespread use across a range of applications, from biomedical [2–4] to space/aerospace fields [5]. Yttria-stabilized tetragonal zirconia polycrystal (Y-TZP), in particular, is widely employed in prosthetic dentistry due to its excellent biocompatibility, superior strength and ability to withstand masticatory forces [6]. Y-TZP major drawback is its susceptibility to low temperature degradation (LTD), a phenomenon that involves the gradual transformation of the tetragonal phase to the monoclinic one, in the presence of moisture, leading to surface roughening, microcracking, and ultimately reducing mechanical performance and stability [6–8]. This degradation, triggered by the presence of oxygen vacancies introduced upon substitution of Zr^{4+} with Y^{3+} ions, can be mitigated by the use of alternative stabilizers, such as cerium oxide, as the Ce^{4+} ions do not generate additional oxygen vacancies within the zirconia lattice [8].

While ceria-stabilized zirconia (Ce-TZP) ceramics exhibit superior fracture toughness [9] compared to Y-TZP, it is characterized by moderate flexural strength [9,10], due to its coarser microstructure. To overcome this limitation, research is increasingly focused on Ce-TZP-based composites, where properly designed second phases can provide ceramics with an exceptional combination of properties, such as flexural strength higher than 1000 MPa, fracture toughness higher than 10 $MPa\sqrt{m}$, long-term stability and exceptional Weibull modulus close to 60 [11,12]. While Ce-TZP-based ceramics are becoming materials of choice in dental implantology [13–17], their outstanding properties enable their spreading into other technological fields, such as aerospace, where Ce-TZP-based composites have been developed for engine components in unmanned aerial vehicles [18].

Improving performance and reliability of technical ceramics is pivotal to establishing them as materials of choice in demanding technological fields. However, the ability to shape these materials into customized and tailored architectures represents the next frontier for ceramic applications. In this frame, the advent of 3D printing is revolutionizing the fabrication of advanced ceramics, by enabling the creation of highly complex designs with enhanced precision. Among the different 3D printing processes, vat-photopolymerization technologies, i.e. Stereolithography (SL) and Digital Light Processing (DLP), have seen a rapid growth in a number of advanced technological sectors, thanks to the possibility of producing components with complex geometries and high surface finishing, not achievable by traditional manufacturing techniques [19]. Both SL and DLP rely on the interaction of a light source with photosensitive liquid monomers loaded with ceramic particles. The 3D object is built by selectively exposing each bidimensional layer to the radiation at a defined wavelength, inducing the polymerization of the liquid resin into the desired shape [20].

---

* Corresponding author.
E-mail address: bartolomeo.coppola@polito.it (B. Coppola).

https://doi.org/10.1016/j.jeurceramsoc.2025.117512
Received 26 January 2025; Received in revised form 27 April 2025; Accepted 4 May 2025

While the paramount influence of powder characteristics – such as particle size, granulometric distribution, specific surface area, and physico-chemical surface properties – on the features of the sintered components is well-established in conventional ceramic processing across all manufacturing stages [21–23], this understanding is still poorly consolidated in the context of additive manufacturing technologies. In spite it is well-recognized that the ceramic slurries used as feeding material in SL and DLP need careful preparation, requiring the optimization of several factors such as solid loading, particle size and distribution, optical and rheological properties [20,24], a still limited attention is given to the intrinsic properties of the ceramic powders themselves.

Few previous works investigated the role of powder features, such as particle size and morphology, on the fresh properties of the slurry and on the final characteristics of the ceramics. For instance, Xu et al. [25] selected different types of commercially available α-Al_2O_3 powders, characterized by significantly different particle size and morphology, and compared their effect on the stability and viscosity of the slurry and on the microstructural and mechanical characteristics of the sintered ceramics. Yang et al. [26] compared the effect of commercial micrometric spherical and faceted α-Al_2O_3 particles on the slurry viscosity and on the microstructural and mechanical properties of the sintered ceramics. An alternative approach, applied to different types of ceramics, including alumina [27,28], zirconia [29,30], zirconia toughened alumina [31] and hydroxyapatite [32], involves selecting powders with significantly different particle sizes and mixing them in different ratios, to provide slurries with a range of bimodal particle size distributions and to explore the role of these ratios on slurry viscosities and curing depth, as well as on the physical and mechanical properties of the final sintered materials.

Unlike previous studies, this work aims to provide a deeper understanding of the influence of the structural and surface characteristics of a selected ceramic powder across all key stages of the additive manufacturing process, unveiling their impact on the fresh and cured properties of the slurry, as well as on the physical and mechanical properties of the final sintered ceramics. More specifically, the study focuses on the elaboration of ceria-stabilized zirconia ceramics by DLP, by facing two major challenges: on one side, the presence of ceria, responsible of a significant absorbance in the UV photopolymerization range [33]; on the other, the need for grain growth refinement strategies, to optimize the mechanical response of the final materials [34]. In this study, the effect of ball milling process, performed to obtain a finely dispersed powder with controlled submicrometric particle size, and that of a subsequent thermal treatment performed to restore possible physical-chemical modifications induced by the milling process, are deeply investigated. The role of these treatments on powder surface properties, slurries rheology and printability, as well as on the properties of green and sintered ceramics was investigated, with the final goal of reducing printing flaws and improving mechanical properties.

2. Materials and methods

2.1. Materials

Ceria-stabilized zirconia powders supplied by Daiichi Kigenso Kagaku Kogyo Co. LTD (Japan) were selected as the starting materials. Precisely, a 1:1 wt ratio mixture of 10 mol% and 12 mol% ceria-stabilized zirconia (Ce-TZP) was used in order to produce final sintered materials with a stabilizing oxide amount equal to 11 mol%, set in view of the elaboration of Ce-TZP-based composites for structural applications [35,36]. The powders were characterized by a specific surface area in the range 10–15 m^2/g, and a micrometric average particle/agglomerate size, as declared by the supplier [37].

For the preparation of the slurries, a commercial photocurable resin (ADMATEC Europe BV, The Netherlands) was used. It consists of 55–75 wt% aliphatic acrylates, 8–25 wt% acrylate oligomers and 0.1–4 wt% phospine oxide, phenylbis(2,4,6-trimethylbenzoyl) photoinitiator.

A commercial dispersant (Disperbyk-103, BYK Chemie, Germany) was employed to maximize the solid loading of the ceramic powder in the resin and to avoid sedimentation.

2.2. Powders modification and characterizations

Un-milled CEZ powder, here labelled as CEZ-UM**,** was obtained by dispersing 10 mol% and 12 mol% ceria-stabilized zirconia powders, in a 1:1 wt ratio, in acetone, without milling media. After overnight dispersion, the suspension was dried in an oven at 70 °C.

Ball-milled CEZ powder, here labelled as CEZ-BM was obtained by ball-milling the CEZ mixture in acetone for 48 h. Milling conditions were set as follows: 2-mm diameter zirconia spheres, powder-to-sphere weight ratio of 1:6. Particle size distribution was monitored overtime by laser granulometry, until a submicrometric monomodal distribution was achieved. Then, the suspension was dried at 70 °C. Ball-milling was carried out to reduce the starting particle size, with the aim of achieving a sintered material characterized by a fine and controlled microstructure and with optimized mechanical properties [38].

CEZ-BM powder was further submitted to a thermal treatment carried out at 600 °C for 1 h, providing powders labelled as CEZ-BM-600**.** This treatment was carried out to restore possible physical modifications induced by milling on the powder surface [39–41].

All powder batches were sieved below 125 µm to remove agglomerates and stored in a dry place until slurry preparation.

The particle size distribution of the three powder batches was assessed by laser granulometry (Mastersizer 3000, Malvern Panalytical, Worcestershire, UK).

The phase composition was investigated by X-Ray Diffraction analysis (XRD) in the 2θ range 5–70° (Empyrean Series 3, Malvern Panalytical; operating parameters: 0.007° step size, 22.95 s fixed counting time per step). Tetragonal and monoclinic zirconia phases were identified by JCPD file n° 82–1398 and 74–0815, respectively. The intensities of the monoclinic $I_{m,1}$ (-111) and $I_{m,2}$ (111) peaks centered at $2\theta = 28.050°$ and $2\theta = 31.333°$, respectively, and the I_t (101) tetragonal peak, centered at $2\theta = 30.0368°$ were used as input values in Toraya's model [42] for determining the weight and volumetric fraction of monoclinic phase.

Fourier-transform infrared spectroscopy (FT-IR) was performed to investigate powder surface modifications resulting from the ball-milling and thermal treatment processes. FT-IR spectra were acquired using ATR mode and all data were recorded as 32 scans with a spectral resolution of 4 cm^{-1} in the range of 4000–525 cm^{-1} (Thermo Scientific Nicolet iS50 FTIR spectrometer, Thermo Fisher Scientific, Milano, Italy).

X-ray photoelectron spectrometry (XPS) was used to characterize the physicochemical properties of the powders. Spectra were collected on a PHI-5000 Versaprobe instrument (Physical Electronics, Chanhassen, MN, USA) equipped with a monochromatic Al Kα source (1486.6 eV) operated at a power level of 120 W. The analysis area was equal to 300×700 μm^2. High-resolution spectra were recorded at a pass energy of 20 eV. Binding energies were calibrated by assigning the adventitious carbon C1s peak to 284.8 eV. Curve fitting was performed using a Gaussian/Lorentzian (70/30) peak shape after Shirley's background subtraction and using X-vison 2.2.11 software.

Transmission electron microscopy (TEM) was carried out using a TALOS F200X G2-Thermo Scientific instrument. The analysis was conducted in HRTEM mode using an electron acceleration of 200 kV. Images were collected by a CMOS camera (Ceta, 16 Mpxl), provided by the producer.

Specific Surface Area (SSA) of CEZ powders was characterized by nitrogen adsorption at 77 K, according to the Brunauer, Emmet and Teller (BET) method. Analyses were carried out by using the Micromeritics Smart VacPrep equipment as the degassing system, and the TriStar II Plus (Surface Area and Porosity Analyzer TriStar 3000 by

Micromeritics, Norcross, GA, USA) as gas adsorption analyzer. Prior to analysis, the powders were degassed at 250 °C for 24 h; around 1 g of powder for each CEZ sample was analysed.

2.3. Slurry elaboration and characterization

Slurries based on CEZ-UM, CEZ-BM and CEZ-BM-600 powders were prepared by stepwise addition of the powders to the liquid resin under continuous stirring in the presence of a commercial dispersant (Disperbyk-103, BYK Chemie, Germany). For all the investigated powders the solid loading was fixed as 80 wt% (corresponding approximately to 41 vol%). Slurries were then submitted to planetary milling (Fritsch Pulverisette, Fritsch GmbH, Germany) with 10-mm diameter agate sphere, by performing three cycles for 1 h at 350 rpm. Before printing, slurries were subjected to degassing for 1 h under vacuum to facilitate the evacuation of trapped air.

The rheology of the slurries was investigated at 25 °C by means of a rotational rheometer (Kinexus Pro+, Netzsch Gerätebau GmbH, Selb, Germany) equipped with stainless steel parallel plates (20 mm diameter) with a 1 mm gap between plates, working in a strain-controlled mode applying shear rates between 0.1–1000 s^{-1} with a logarithmic progression taking 10 samples per decade (sampling time of approx. 6 s).

2.4. Printing and post-processing

Samples with different geometries were designed using the AutoCAD software and printed using a DLP printer (ADMAFLEX 130, ADMATEC Europe BV, The Netherlands), operating with a 405 nm wavelength UV light and an adjustable tape transport speed between 10 and 20 mm/s, on which the photocurable slurry is spread by a doctor blade with a gap size of 125 μm. Therefore, the operative shear rate of the printing jobs was calculated between 80 and 160 s^{-1}, thus the average value of 120 s^{-1} was considered.

Before each printing job, curing depth was evaluated through dedicated projection tests performed by combining different exposure parameters sets, i.e. exposure time and led power, to find the most convenient compromise among high resolution, adhesion to the building platform and layer uniformity. The thickness of the single layer was measured with a digital micrometer.

Printed samples were thoroughly cleaned under deionized water flow using a soft brush to remove exceeding uncured resin from the samples surface. Then, samples were subjected to water debinding by immersion at 30 °C overnight. Drying was finalized at room temperature in wet environment for at least 4 h and then in dry conditions for 24 h. Thermal debinding was performed in an electric furnace (Carbolite 1800, Carbolite Gero GmbH) under air atmosphere, according to conditions previously reported [36,43].

2.5. Characterization of the printed samples

Dilatometric tests were performed to investigate the sintering behaviour of as-printed bars (LxSxH: 15x5x5 mm^3) to support the definition of proper sintering cycles. Geometrical density and Archimedes' density were determined on green and sintered samples, and related to material theoretical density, considering values of 6.23 and 5.74 g/cm^3 (obtained from the tetragonal and monoclinic zirconia phases JCPD files n° 82–1398 and 74–0815) for tetragonal and monoclinic zirconia, respectively.

Microstructural characterization of sintered samples was carried out by Field Emission Scanning Electron Microscopy (FESEM - Hitachi, Tokyo, Japan) performed on polished and thermally etched surfaces. Grain size was determined by image analysis using a commercial software (Scandium by Soft Image System).

The flexural strength of sintered samples (as-printed, i.e. without any grinding and polishing process) was determined via three-point bending tests using an electromechanical testing system (Zwick Roell 2014, Ulm, Germany) equipped with a load cell of 50 kN. A crosshead speed of 1 mm/s and a support span of 20 mm were used. Samples were tested with the loading direction parallel to the printing one, testing at least five samples per each type and sintering temperature.

3. Results and discussion

3.1. Preliminary characterizations of the powders

In Fig. 1, the granulometric curves of CEZ-UM, CEZ-BM and CEZ-BM-600 powders are depicted, showing both the particle size (solid line) and the cumulative (dashed line) distributions. CEZ-UM was characterized by an almost monomodal and narrow distribution (black curve), centred at about 3 μm. Ball milling produced an effective dispersion of the powder, since CEZ-BM (red curves) showed a significant displacement towards nanometric particle sizes, showing the almost monomodal curve centred at about 0.2 μm. The ball-milled and calcined powder (CEZ-BM-600, blue curves) maintained almost the same distribution as the CEZ-BM powder, indicating no re-agglomeration during the thermal treatment. For sake of clarity, the particle sizes corresponding to 10 % (D_{10}), 50 % (D_{50}) and 90 % (D_{90}), determined from the cumulative distribution curves, are shown in the same Figure.

In Fig. 2, TEM analyses of the CEZ-UM (a,d), CEZ-BM (b,e) and CEZ-BM-600 (c,f) powders are depicted. Comparing lower (a-c) and higher (d-f) magnifications images, the different degree of agglomeration can be appreciated: while CEZ-UM shows large agglomerates of ultrafine powders, entrapping a submicronic-sized porosity, the milled materials, both CEZ-UM and CEZ-BM-600 powders, show small packets made by a restricted number of particles, or even individual particles. In line with granulometric data, ball-milling resulted to effectively promote powder dispersion by de-agglomerating the starting large particle packets, and

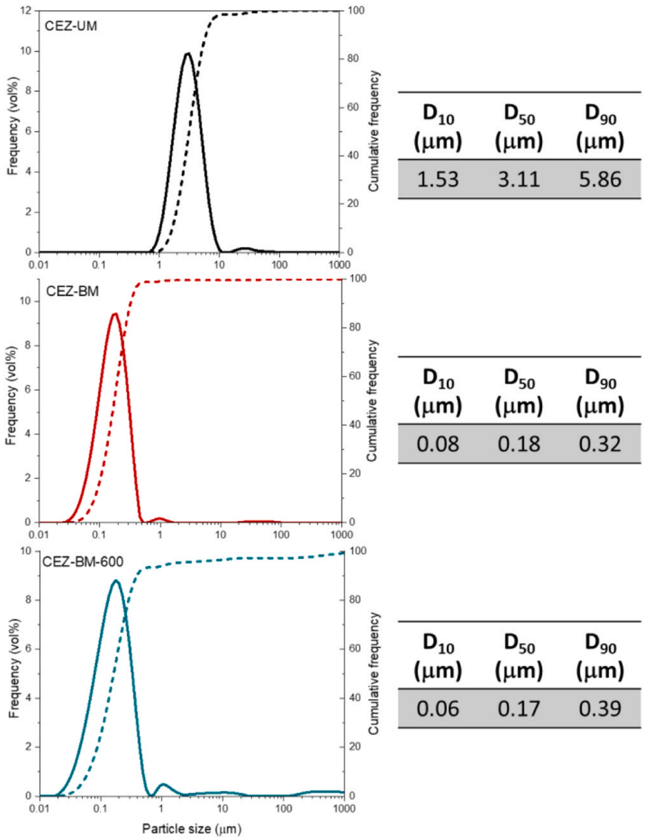

D_{10} (μm)	D_{50} (μm)	D_{90} (μm)
1.53	3.11	5.86

D_{10} (μm)	D_{50} (μm)	D_{90} (μm)
0.08	0.18	0.32

D_{10} (μm)	D_{50} (μm)	D_{90} (μm)
0.06	0.17	0.39

Fig. 1. Particle size (solid line) and cumulative (dashed line) distribution curves of CEZ-UM, CEZ-BM and CEZ-BM-600. On the right, D_{10}, D_{50} and D_{90} values, derived from the cumulative distributions, are collected.

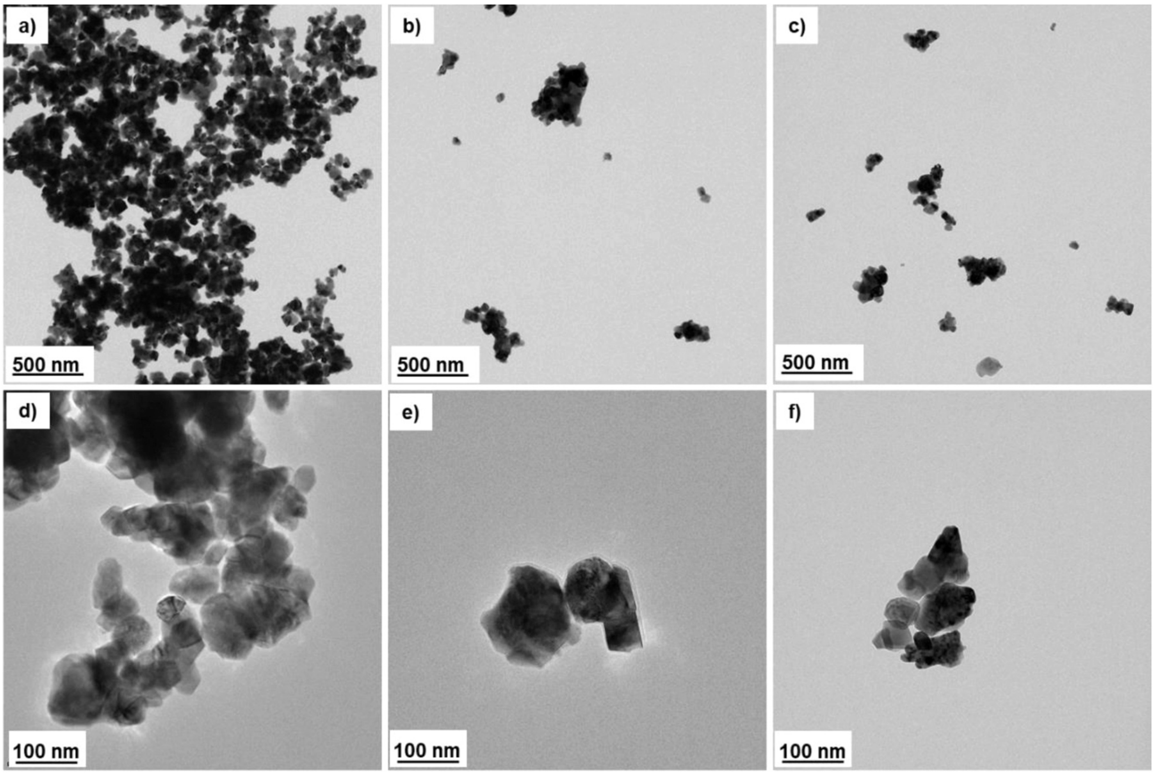

Fig. 2. TEM micrographs of CEZ-UM (a-d), CEZ-BM (b-e) and CEZ-BM-600 (c-f) powders.

no re-agglomeration occurred after the calcination step.

In Fig. 3, the XRD patterns of the powders are depicted. CEZ-UM was characterized by a significant fraction of the monoclinic zirconia phase, corresponding to 55.4 vol%, in agreement with a previous literature study [44]. This fraction further increased after the ball-milling step in CEZ-BM, reaching the value of 84.2 vol%. Finally, the thermal treatment carried out on the ball milled powder (CEZ-BM-600) induced a significant decrease of the monoclinic phase, reaching 32.1 vol%.

The effect of milling on the martensitic phase transformation of zirconia powder has been already described in the literature. Lakusta et al. [45] investigated a 3 mol% yttria-stabilized zirconia powder containing a starting 4 % of monoclinic phase. The authors showed a progressive increase (up to about 31 %) of monoclinic zirconia after planetary milling for 8–48 h, and imputed the *t*-to-*m* transformation to microscale stress and strain introduced into the zirconia lattice by the mechanical energy of the milling process. Similarly, Skovgaard et al. [46] determined a progressive transformation of tetragonal zirconia into the monoclinic one by increasing the ball milling time, and showed that the transformation rate increased by increasing the milling rate. Anyway, they demonstrated that even mild milling condition (such as 120 rpm for 1 h, ∅ = 0.5 mm balls) was enough to induce phase transformation. A last reference is given by Lin and Duh [47]; in this case, 2 mol% Y_2O_3-5.5 mol% CeO_2-ZrO_2 powders were obtained by co-precipitation and ball-milled in ethanol, again demonstrating a monoclinic phase increase from 8.3 to 13.2 vol% after 12 h of milling.

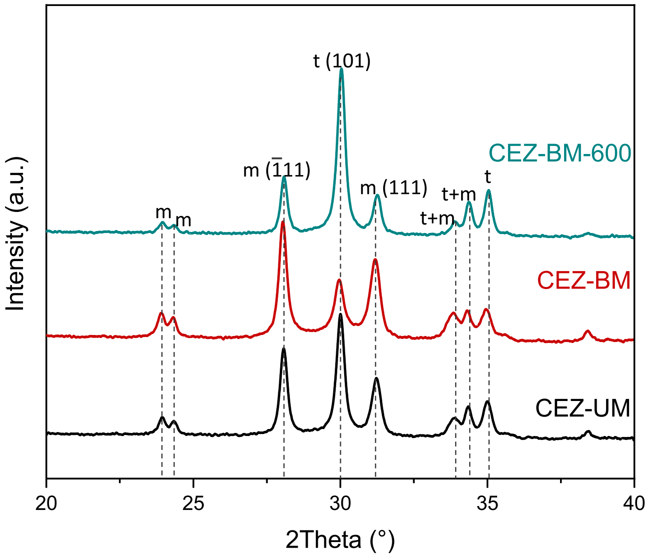

Fig. 3. XRD patterns of CEZ-UM, CEZ-BM and CEZ-BM-600.

While ball-milling induced an increase of the monoclinic phase, the thermal treatment at 600 °C had the opposite effect, reducing the monoclinic zirconia content. This result agrees with previous studies [48,49], showing the transition of monoclinic ZrO_2 to the higher temperature-stable tetragonal phase, as a consequence of the calcination process.

3.2. Slurry optimization and printing

In Fig. 4 the rheological curves of the CEZ-UM, CEZ-BM and CEZ-BM-600 slurries, prepared at 80 wt% solid loading, each of them at optimized dispersant amount, in the range 2–3 % as respect to the zirconia powder, are collected. In particular, to provide printable slurries, 2 wt% was used for CEZ-UM slurry while 3 wt% for CEZ-BM and CEZ-BM-600 slurries. The curves show a shear-thinning behaviour, with a clear decrease of the shear viscosity by increasing the shear rate. In addition, from the rheological curves, shear rates at some key shear viscosities have to be taken into account (light blue lines in the figure), and precisely the values at the (almost) null shear rate ($\dot{\gamma} = 0.02\ s^{-1}$) and that at the operative shear rate ($\dot{\gamma} = 120\ s^{-1}$), as defined in the experimental section. Shear viscosities at these values are shown in the table included in Fig. 4. Both values are critical for ensuring optimal slurry printability:

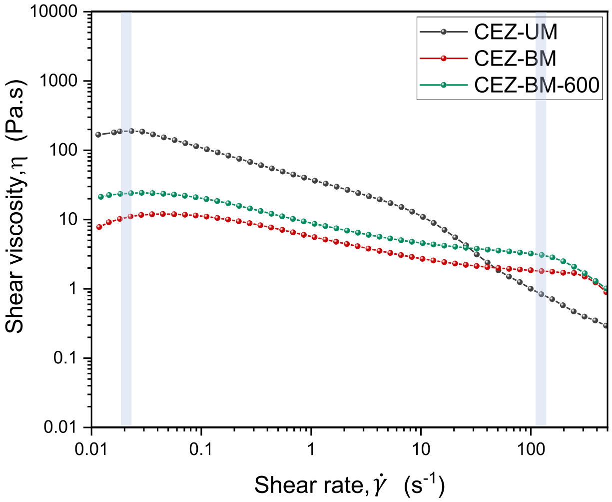

	Shear viscosity (Pa.s) @ $\dot{\gamma}$ = 0.02 s^{-1}	Shear viscosity (Pa.s) @ $\dot{\gamma}$ = 120 s^{-1}
CEZ-UM	200	0.86
CEZ-BM	11.1	1.85
CEZ-BM-600	23.7	3.07

Fig. 4. Rheological curves of the slurry at 80 wt% for CEZ-UM (black), CEZ-BM (red) and CEZ-BM-600 (green) powders. On the right, the table collects the shear viscosity values at the shear rates of 0.02 s^{-1} and 120 s^{-1}.

the former indicates the slurry viscosity during the degassing stage, and while the platform descends onto the slurry deposited on the tape, leading to entrapped air to be removed; the second value is essential during the blade-assisted spreading of the slurry onto the tape. For the latter parameter, low viscosity values, typically lower than 3–5 Pa.s, are recommended in the literature [26]. While the three slurries presented very low viscosities at the operative shear rate, especially for CEZ-UM, the same slurry showed the highest value at $\dot{\gamma} = 0.02$ s^{-1}, probably due to the presence of bigger particles in the resin, resulting in high friction compared to the other slurries. However, as the level of shear stress is gradually increased, the powder agglomerates respond to the applied stress by decreasing their size and aligning themselves in the flow direction, leading to a marked viscosity decrease [50,51]. CEZ-BM and CEZ-BM-600 showed a similar behaviour: the former slurry was just displayed at slightly lower values compared to the latter, suggesting a not critical role of calcination on the slurry viscosity.

In Fig. 5 (a), the relation between the curing depth (C_d) and the exposure energy for the three different slurries is provided. First, all the slurries showed an expected increase of C_d by increasing the exposure energy. In addition, they experienced low C_d values, in the range 15–35 μm, that can be ascribed to the significant absorbance of ceria at the operative wavelength (405 nm) [33], interfering with the light penetration in the slurry, consequently reducing the photo-polymerization behaviour. Furthermore, the occurrence of light scattering at the particle-resin interface due to their different refractive indexes (RI) must be considered as well. In fact, while a common DLP resin shows RI of around 1.5 [20], ceria-zirconia mixed oxide particles are characterized by RI (at around 400 nm) of ≅ 2.2 [52] indicating a significant mismatch, and thus a high scattering amplitude function [53].

In addition, one can observe that CEZ-UM and CEZ-BM slurries were characterized by lower C_d values compared to CEZ-BM-600, in the whole energy range. Furthermore, in the investigated exposure energy range, the slope of the line fitting CEZ-BM data is lower compared to CEZ-UM one, leading to even lower C_d values especially for high exposure energy. The powder particle size and its dispersion degree into the resin are known to affect the scattering phenomena of the UV light, responsible of the photopolymerization, since smaller particles improve the scattering effect. Our results indicate that such scattering does not provide any increase in curing depth. On the opposite, it is reasonable to assume that scattering delivers more radiation in sideway directions and enlarges the curing width (C_w), providing reduced resolution [20]. For these two slurries, optimal printing conditions were set at 650 mJ/cm^2, to achieve a C_d of around 25 μm.

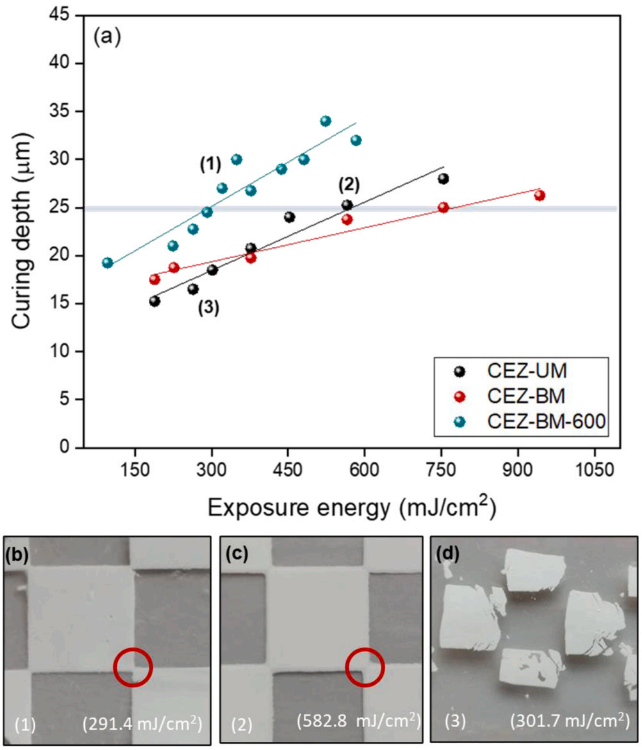

Fig. 5. a) Curing depth vs exposure energy for CEZ-UM, CEZ-BM and CEZ-BM-600 slurries; b-d) representative pictures of the chessboard tests corresponding to points (1), (2) and (3) in Fig. 5a. Red circles highlight the different printing accuracy of the chessboard vertexes.

The CEZ-BM-600 slurry behaved differently: in fact, curing depths values are shifted at significantly higher values. While a previous work showed that surface modification of ceramic particles had a clear effect on the curing depth [54], in this paper further surface and structural characterizations, reported in the next section, are provided with the aim of better understanding this difference. Anyway, according to the results shown in Fig. 5a, it was possible to keep the same $C_d \cong$ 25 μm as for the previous slurries, but by using a much lower energy, corresponding to 300 mJ/cm^2. Therefore, for all the investigated slurries the layer thickness was set at 15 μm, avoiding delamination phenomena during 3D printing by ensuring a C_d at least 1.5 times the imposed layer thickness.

In Fig. 5(b-d) representative photos of the chessboard tests, performed at selected C_d/exposure energy values (numbers 1–3 in the Fig. 5a), are depicted. In particular, in Fig. 5b (corresponding to point 1), we can observe the square obtained for CEZ-BM-600 at ≅ 300 mJ/cm^2, showing that it is well defined (see the vertex) and fully cured. In Fig. 5c (corresponding to point 2), the square underwent evident overcuring phenomena, as observable by the (overgrowth) square [55,56] characterized by loss of resolution, as again evident in the vertex. These results agree with previous literature [54,57] that investigated the relationship between the energy dose and the curing width (C_w) showing a progressive increase in C_w by increasing the exposure energy. Moreover, such squares resulted to be more brittle compared to the ones obtained by the previous slurry, as it tended to break upon handling. Attempts to reduce the exposure energy for CEZ-UM and CEZ-BM slurries were unsuccessful (point 3) since the low penetration depth, led to uncomplete curing, and the squares disintegrated during the removal of the excess resin (Fig. 5d).

Under the above-defined printing conditions, bars derived by the three slurries were printed and submitted to water debinding, necessary to remove the uncured slurry. Powder pre-treatment significantly affected the samples quality at this processing step, as shown in Fig. 6: in fact, CEZ-UM was characterized by printing flaws mainly localized at the samples edges and borders (Fig. 6a). On the other side, CEZ-BM presented an important delamination, affecting the whole sample length, and limiting any further material processing (Fig. 6b). On the opposite, the ball-milling and calcinations steps carried out on CEZ-BM-600 were effective in strongly reducing flaws appearance and avoiding delamination, allowing the fabrication of compact materials (Fig. 6c). In Fig. 6d, a digital image of CEZ-BM dilatometric bar is depicted, further showing that delamination occurred in the whole sample length, while in Fig. 6e, CEZ-BM-600 water debinded samples are shown, exhibiting regular geometry and delamination-free samples.

3.3. Additional surface and structural characterizations of the powders

With the aim of deepening the role of powders pre-treatments on slurries printability, additional surface and structural characterizations were carried out. Ball milling was responsible for a particle size reduction of the starting powder to a submicrometric/nanometric scale, likely potentially resulting in increased specific surface area (SSA), with possible effects on UV light scattering phenomena [20]. In our case, just a slight change in specific surface area was observed upon the different treatments: in fact, CEZ-UM was characterized by a SSA of 12.79 m^2/g, that increased to 13.82 m^2/g for the CEZ-BM powder, and then slightly decreased to 13.00 m^2/g in CEZ-BM-600 sample confirming what previously discussed in relation to TEM micrographs (Fig. 2).

In Fig. 7, the FTIR spectra of the three powders are compared. The spectrum at wavelength < 1000 cm^{-1} (not shown) is typically related to the Zr-O metal-oxygen bonding [58]. The grey dash lines highlight the areas where the strongest differences among the powders can be observed. In particular way, the strong absorption band in the range between 3000 and 3600 cm^{-1}, and centred at ≅ 3400 cm^{-1}, is due to the hydroxyl stretching vibration, and thus to OH species present on the

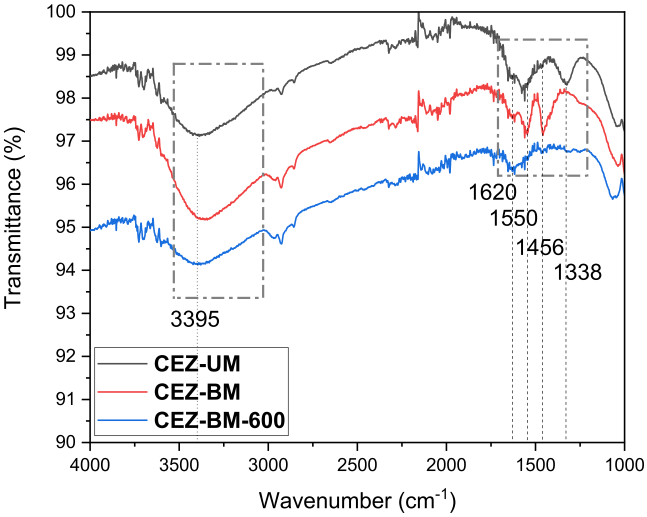

Fig. 7. FTIR spectra of CEZ-UM, CEZ-BM and CEZ-BM-600 powders.

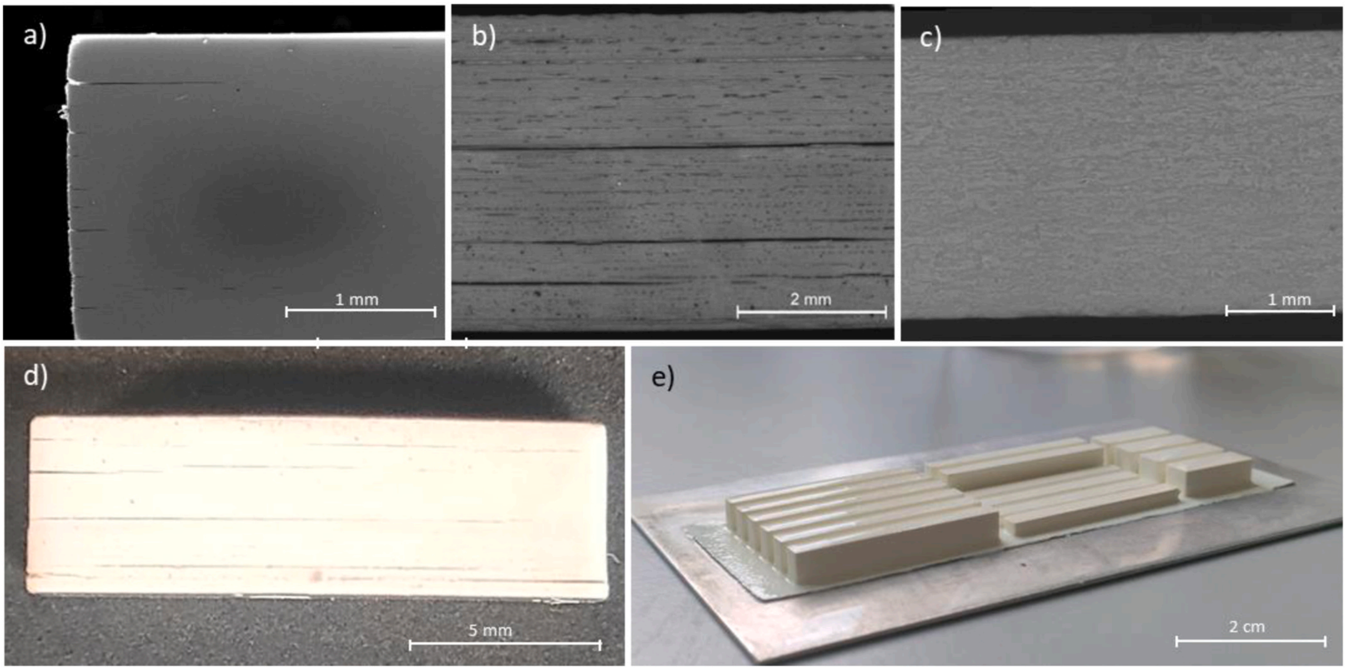

Fig. 6. FESEM micrographs of sample section after water debinding: a) CEZ-UM; b) CEZ-BM and c) CEZ-BM-600; digital photographs after water debinding of: d) CEZ-BM dilatometric bar, showing delamination in the whole sample length; e) CEZ-BM-600 samples, showing regular bars with no delamination.

surface [58–60]. It can be easily observed that such absorption band showed the highest intensity in the CEZ-BM material, while it decreased significantly after thermal treatment at 600 °C. This indicates the occurrence of a hydrated surface, especially in the milled, ultrafine material, and an effective dehydroxylation after thermal treatment. Such hypothesis is strengthened by the peak located at 1456 cm^{-1}, present solely in the CEZ-BM powder, and associated to hydroxyl groups [61]. The peak at 1620 cm^{-1} can be attributed to the asymmetric stretching behaviour of Ce-O [62] while the signals at 1550 cm^{-1} and 1338 cm^{-1} present in the CEZ-UM and/or CEZ-BM materials, can be associated to the vibration of νC═O and δCH species, related to adsorbed acetone on zirconia and ceria surface at room temperature [63], and not present in the thermally treated powder.

Still with the aim of investigating the surface physical-chemical properties, XPS analyses were performed as well, and results are shown in Fig. 8. In particular way, high-resolution spectra for O1s and Zr3d are depicted. O1s can be deconvoluted into three components, with maxima located at ≅ 529.5, 531.7, and 533.2 eV, respectively. According to the literature on zirconia and ceria-zirconia mixed oxides [64–69], these peaks are attributed to oxygen in the lattice network (indicated as O-Zr in the Figure), oxygen related to surface hydroxyl species (OH-Zr), and oxygen related to adsorbed water (H_2O-Zr), respectively [64,65,70]. CEZ-UM and CEZ-BM samples were characterized by similar features, with comparable intensity of the peaks corresponding to the above-mentioned three components. On the contrary, the spectrum of CEZ-BM-600 was significantly different, in terms of peaks energy and intensity. In fact, a shift of ≅ 0.2 eV towards higher binding energy was determined, while a strong decrease of the peak intensity related to hydroxyl species (OH-Zr) and the disappearance of the signal related to adsorbed water (H_2O-Zr) were observed.

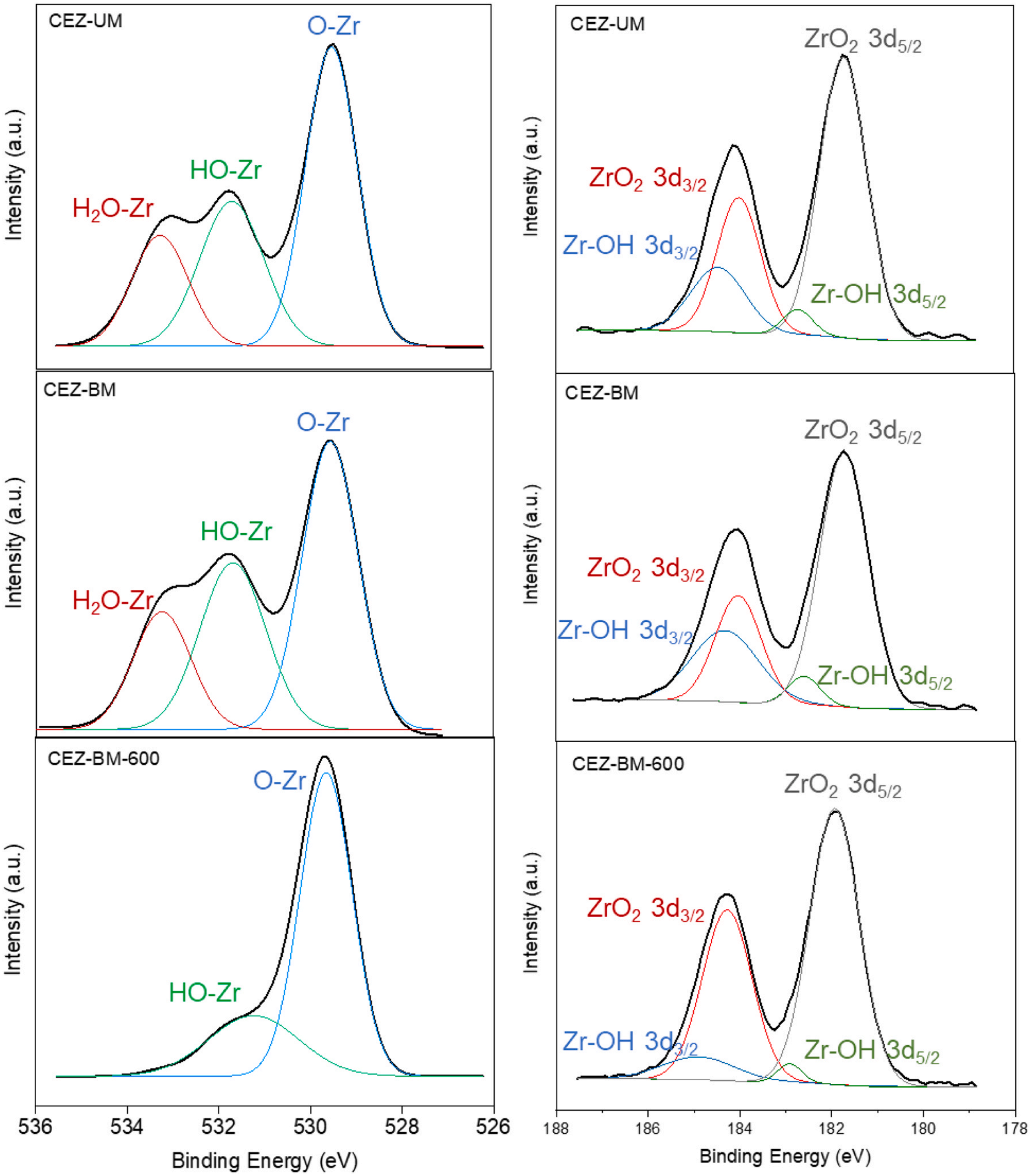

Fig. 8. XPS spectra and related deconvolution curves of O1s and Zr3d, for CEZ-UM, CEZ-BM and CEZ-BM-600 powders.

The deconvolution of the Zr3d spectrum evidenced four contributions: the doublet at around 181.6 (Zr $3d_{5/2}$) and 184.1 eV (Zr $3d_{3/2}$) is due to ZrO_2 and/or CeO_2-ZrO_2 mixed oxides, so to lattice zirconia and ceria (indicated in the figure as ZrO_2 $3d_{5/2}$ and ZrO_2 $3d_{3/2}$), while the second doublet located at 182.2 (Zr $3d_{5/2}$) and 184.8 eV (Zr $3d_{3/2}$) arises from zirconium hydroxide (in the Figure, Zr−OH $3d_{5/2}$ and Zr−OH $3d_{3/2}$) [61,67]. Also in this case, it is possible to observe a certain difference of the surface state of CEZ-BM-600 powder; in fact, the peaks were characterized by the same shift of about 0.2 eV towards higher binding energy, and a certain decrease of the hydroxyl species and adsorbed water.

In literature, the shift of the peaks is related to the oxidation state of the analysed elements, where higher oxidation states generally result in a higher binding energy [71,72]. The shift occurs because the oxidation process changes the electron density around the cerium and zirconium atoms, thus altering its interaction with the photoelectron being ejected. The slightly reduced state of the zirconia can correspond to the presence of oxygen vacancies, as demonstrated in previous literature. Sinhamahapatra et al. [73] fabricated an oxygen-deficient black ZrO_{2-x} material, that showed Zr3d peaks located at a binding energy ≅ 0.4–0.6 eV lower than the corresponding material in which the oxygen vacancies were restored by oxidation process. Similarly, Dashtbozorg et al. [74] prepared an oxygen deficient ZrO_{2-x} material by plasma treatment and carried out a XPS characterization to investigate the concentration of oxygen vacancies. The authors deconvoluted the O1s peaks into three signals, associated to lattice oxygen, surface adsorbed hydroxyl groups and surface adsorbed molecular water, in line with our research. They observed a limited, but existing, shift of 0.1–0.2 eV of the three peaks towards higher binding energy, moving from the plasma treated reduced material to the untreated one.

In this work, the formation of oxygen vacancies can be reasonably imputed to the cerium reduction from tetra- to tri-valent state, due to the well-known easy Ce^{4+}/Ce^{3+} conversion [75]. Here, the high-resolution XPS analysis of the cerium peak has not been reported, since its relatively low amount into zirconia makes the spectrum poorly resolved, and the photoreduction effect during analysis [65] can lead to incorrect or understandable results. In spite of this, one can reasonably assume that in the UM and BM materials, a certain amount of reduced cerium ions is present, as associated to oxygen vacancies, while the thermal post-treatment was able to restore a fully oxidized surface. To strengthen this hypothesis, previous literature indicated that CeO_2 powder submitted to mechanochemical process underwent ceria reduction, with formation of oxygen vacancies as well as other bulk and surface defects [76–78]. On the opposite, the calcination treatment was effective in restoring Ce^{3+} into the tetravalent form [79,80].

In Table 1, the results of the surface elemental analysis as well as the quantification of the species determined by the deconvoluted areas of O1s and Zr3d peaks are collected. A decreasing Ce/Zr ratio was observed moving from the CEZ-UM, to CEZ-BM and finally to CEZ-BM-600, suggesting that both milling and calcination treatment can favour the solubility of ceria inside zirconia, reducing possible ceria segregation on the zirconia surface [81,82]. Further, a lower oxygen/metal cation ratio (O/Ce+Zr) was determined in CEZ-BM-600 powder compared to the other samples, despite oxygen vacancies annihilation due to thermal treatment. This can be explained by considering the ratio between surface adsorbed hydroxyl groups and lattice oxygen (O1s - HO-Zr/O-Zr) or surface adsorbed molecular water and lattice oxygen (O1s - H_2O-Zr/O-Zr), significantly higher in the un-calcined powders, underlying the need of the thermal post-treatment to eliminate surface hydroxyls and adsorbed water, meaning that the water molecules do not desorb easily, but form a stable layer that remains bound to the surface (referred to as irreversibly adsorbed water), according to literature [83,84].

Table 1

Data from surface elemental analysis and from quantification of the deconvoluted areas of O1s and Zr3d peaks.

	CEZ-UM	CEZ-BM	CEZ-BM-600
Ce/Zr (at%)	11.5	12.2	9.5
O/Ce+Zr (at%)	3.7	3.6	2.3
O1s - HO-Zr/O-Zr[a]	59.5	67.9	34.5
O1s - H_2O-Zr/O-Zr[b]	40.1	42.1	n.d.
$Zr3d_{5/2}$ - HO-Zr/ZrO_2[c]	5.7	7.2	3.2
$Zr3d_{3/2}$ - HO-Zr/ ZrO_2[d]	59.1	96.3	19.6

[a] Surface hydroxyls/lattice oxygen ratio.

[b] Adsorbed water/lattice oxygen ratio.

[c] Surface hydroxyls/lattice zirconia ratio for $Zr3d_{5/2}$.

[d] Surface hydroxyls/lattice zirconia ratio for $Zr3d_{3/2}$.

In summary, the additional structural and surface characterizations of the powders allowed to formulate some hypotheses, that anyway deserve further investigations.

In particular way, the different surface features can be taken into consideration to explain the lower curing depth of both CEZ-UM and CEZ-BM slurries compared to the CEZ-BM-600 one. In fact, both the segregation of ceria on the zirconia surface and the presence of surface oxygen vacancies increase the UV light absorbance [73].

The higher UV absorbance in CEZ-UM and CEZ-BM implied much higher energy dose to achieve the same curing depth as CEZ-BM-600. Such high exposure energy induced overcuring, leading to internal residual stresses, as previously assessed by other authors [85–87]. It can be hypothesized that when immersed in water for debinding, the hardened materials underwent some shrinkage and bending, favouring the delamination in the overcured materials. On the opposite, in the less cured and less brittle CEZ-BM-600, the same dimensional and shape changes did not induce any loss of integrity.

The presence of adsorbed water on the surface of unmilled and milled zirconia powders, effectively removed by the thermal treatment in CEZ-BM-600, was clearly demonstrated by FTIR and XPS analyses. While such hydroxyl groups and surface water do not interfere with the acrylic resin photopolymerization [88], they can play a role in modifying the slurry viscosity: in our case (see Fig. 4), no detrimental effect due to surface hydroxyl species can be determined; a lower viscosity was observed for the CEZ-BM slurry compared to CEZ-BM-600 one. The latter aspect could be related to the ability of the used dispersant, namely a solution of polyester phosphoric acid ester salt [89], to bind to the OH surface groups through its phosphate anchoring head [51], meaning a more effective interaction with the BM particles due to their richer OH environment.

3.4. *Sintering and mechanical characterization*

Due to flaw and delamination appearance, CEZ-BM printed samples were no further processed. On the opposite, the less defective (CEZ-UM) and no-defective (CEZ-BM-600) samples were submitted to dilatometric analysis to optimize the sintering cycle. Small printed bars (15x5x5 mm^3), characterized by a green density of 3.06 g/cm^3 (in the printed form, i.e., considering both the resin and the ceramic powder), were analysed by dilatometry carried out at 1525 °C for 1 h, as shown in Fig. 9a. The small shrinkage (in the range 1–2 %), determined at around 200 °C is caused by the polymer binder burn-out. Then, it is possible to observe that the CEZ-BM-600 curve is shifted to slightly lower temperatures compared to CEZ-UM: in fact, onset sintering temperatures occur at around 1000 °C and 1025 °C, respectively, while the temperatures of the maximum densification rate (determined by the derivative curves) are located at 1189 °C and 1215 °C, respectively. The total linear shrinkage was similar for both samples, corresponding to about 25.6 %.

According to these results, samples were first densified at 1500 °C for 1 h, reaching the final Archimedes' density of 98.3 ± 0.7 % and 99.0 ± 0.8 % for CEZ-UM and CEZ-BM-600, respectively. In Fig. 9b and c, FESEM micrographs of the two sintered materials are depicted, showing a coarser microstructure in the case of CEZ-BM-600 specimen. In fact, a mean grain size of 1.81 ± 0.65 µm for CEZ -UM and 2.57 ± 0.99 µm for

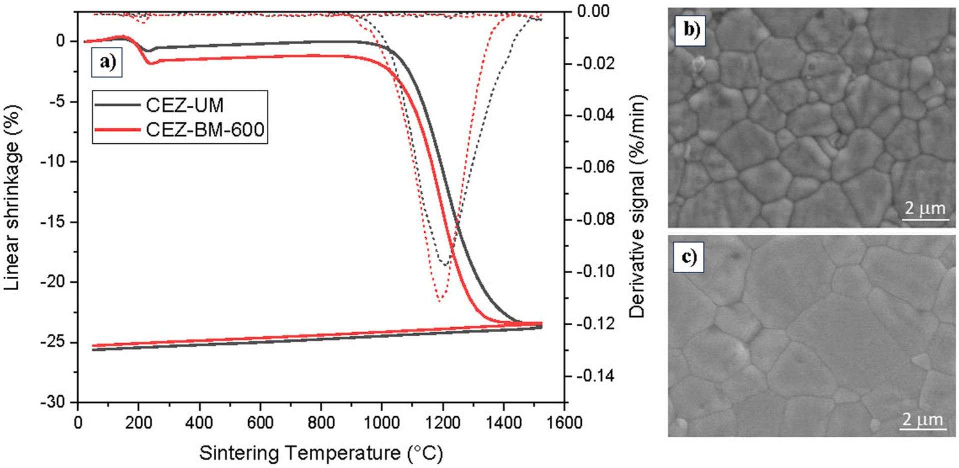

Fig. 9. Dilatometric and derivative curves of CEZ-UM and CEZ-BM-600 sintered at 1525 °C for 1 h (a); FESEM micrographs of CEZ-UM (b) and CEZ-BM-600 (c) sintered at 1500 °C for1 h.

CEZ -BM-600 was determined by image analysis. CEZ -BM-600, from around 1400 °C onward, was characterized by an almost null linear shrinkage, meaning that only grain growth occurred in that temperature range. Such coarsened microstructure was accompanied by a significant increase of the monoclinic zirconia phase percentage (V_m), from 43 vol % in CEZ-UM to 78 vol% in CEZ -BM-600.

Preliminary flexural strength tests, carried out by 3-point bending equipment on prismatic bars, provided a value of 357 ± 25 MPa for CEZ -UM. In case of CEZ-BM-600, in spite the reduced presence of flaws and delamination compared to the un-milled material, a significant lower value (162 ± 42 MPa) was determined, that can be explained by the larger grain size and higher monoclinic zirconia content in the sintered materials.

In the attempt to improve the CEZ-BM-600 mechanical properties, different sintering cycles were tested, with the aim to achieve the best compromise between high sintering density and low zirconia monoclinic fraction. The best results were obtained after sintering at 1400 °C for 1 h and 1350 °C for 0.5 h, providing final densities of 98.9 ± 0.7 % and 97.3 ± 0.5 % respectively. Results related to sintering temperature, sintered density, monoclinic zirconia fraction and 3-point bending strength are collected in Table 2, while micrographs collected on the fracture surface of CEZ-BM-600 materials sintered at the three temperatures are depicted in Fig. 10. We can observe a progressive change in the fracture mode of the materials: as the grain size increases, a change in the fracture mode from inter-granular to intra-granular can be observed, as already reported in the literature [90,91]. In fact, at the lowest sintering temperature, a prevalently inter-granular fracture is observed, where at higher sintering temperatures, a mixed inter and intra-granular fracture mode can be observed.

The best result in terms of mechanical properties was achieved for CEZ-BM-600 sintered at 1350 °C for 0.5 h, thanks to the combination of high sintered density, low monoclinic fraction and sub-micrometric average grain size. It should be pointed out that this sample provided a macrostrucurally flat fracture surface after failure (Fig. 11) that was further investigated for fractographic analysis (Fig. 12). First, the typical brittle fracture can be recognized by observing the full cross-section after bending (Fig. 12a) with the tensile side at the bottom and the compression curls in the compression side (upper side of the sample) [92–94]. A possible origin of the failure could be detected in the tensile side where a more porous area can be recognized (Fig. 12 b-c).

In this study, the mechanical data serve as complementary information to the previously discussed surface and structural characterizations, while a comprehensive analysis of the mechanical behaviour of the optimally 3D-printed ceramics will be the subject of future investigations.

To the best of authors' knowledge, only two previous studies have investigated the mechanical properties of ceria-stabilized zirconia ceramics processed by vat-photopolymerization techniques [95,96]. However, in both cases, the stereolithography process was supplemented with isostatic pressing, applied either to the green or pre-sintered bodies, reasonably leading to improve the density and refine the microstructure. Specifically, Li et al. [95] used SL to print Ce-TZP specimens, and submitted the green bodies to cold isostatic pressing at 250 MPa for 2 h, before sintering at 1500 °C. Three-point bending tests, carried out with 20 mm span, provided the value of 592 ± 47 MPa. Zhao et al. [96] developed 12Ce-TZP bars by SL, that were pre-sintered at 1000 °C, then pressure-less sintered between 1100 and 1300 °C for 2 h, and finally hot-isostatically pressed at 200 MPa, 1250 °C for 1 h. Three-point bending test (span of 20 mm, 2×1.5×25 mm^3 specimens, polished to meet the requirement of surface quality) provided a flexural strength of approximately 770 MPa. This value was significantly higher than that of the material subjected solely to pressure-less sintering, which exhibited a flexural strength of 521 MPa. Therefore, the mechanical strength achieved in this study is comparable to that reported in previous literature, achieved under the same mechanical test and setup.

A wider analysis of mechanical properties was done including recent literature that pertains to Ce-TZP ceramics fabricated using conventional techniques. Comparison must be done cautiously, as mechanical properties are affected not only by processing parameters—including forming, sintering, and post-processing—but also by the specific flexural testing method employed. Sharma et al. [97] developed 10 −12 mol%

Table 2
Sintered density, monoclinic phase percentage (V_m), mean grain size, and flexural strength of CEZ-UM and CEZ-BM-600 submitted to different sintering cycles.

	Sintering cycle	Sintered density (%TD)	V_m (%)	Mean grain size (μm)	Flexural strength (MPa)
CEZ-UM	1500 °C/1 h	98.3 ± 0.7	43	1.81 ± 0.65	357 ± 25
CEZ-BM−600	1500 °C/1 h	99.0 ± 0.8	78	2.57 ± 0.99	162 ± 42
	1400 °C/1 h	98.9 ± 0.7	16	1.18 ± 0.51	369 ± 24
	1350 °C/0.5 h	97.3 ± 0.5	13	0.60 ± 0.23	561 ± 15

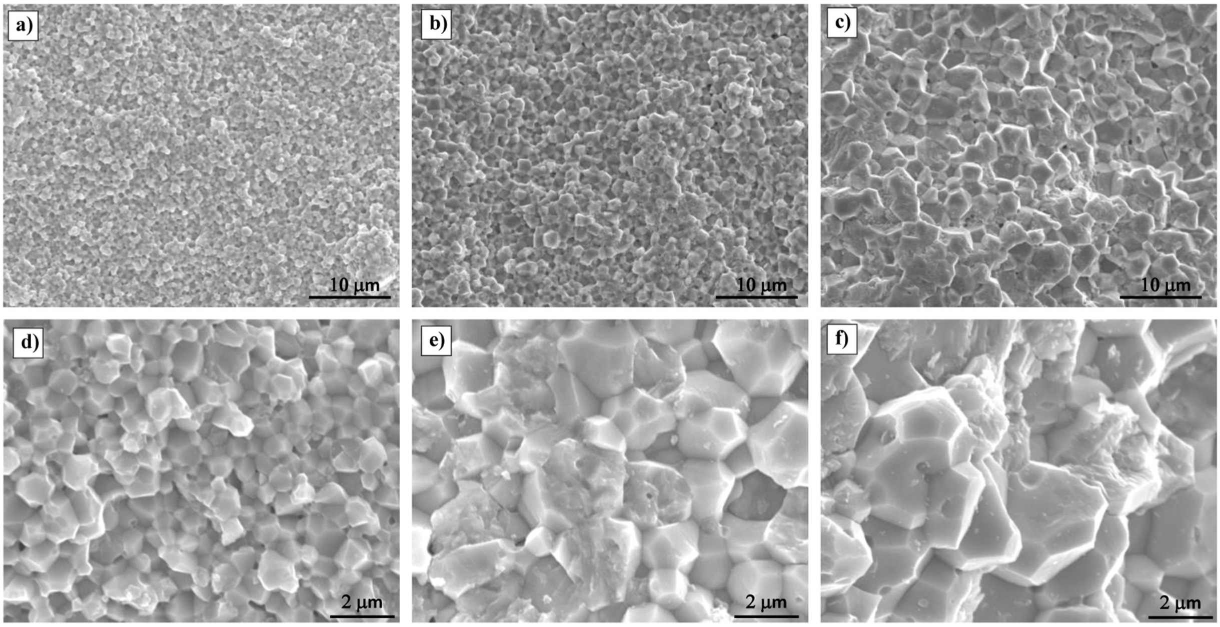

Fig. 10. FESEM micrographs, at different magnifications, carried out on the fracture surfaces of CEZ-BM-600 sintered at 1350 °C for 0.5 h (a,d), 1400 °C for 1 h (b,e) and 1500 °C for 1 h (c,f).

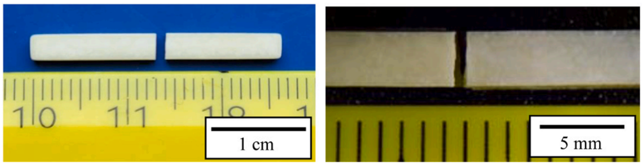

Fig. 11. Optical microscope pictures of CEZ-BM-600 samples (sintered at 1350 °C for 0.5 h) fracture mode after 3-point bending tests.

ceria-stabilized zirconia samples by uniaxial pressing and sintering at 1400 °C for 2 h, achieving an average grain size of around 2 μm and null monoclinic zirconia content. Three-point bending strength tests (span of 20 mm, 2.5 ×3.5 ×30 mm^3 specimens, polished to 1 μm finish), provided values in the range 600–730 MPa. El Attaoui et al. [98] developed Ce-TZP at different ceria contents, including 10 and 12 mol%, and submitted them to uniaxial pressing, followed by isostatic pressing and finally sintering in the range 1430 °C-1450 °C for 2 h, achieving a sintered microstructure characterized by 1.6 μm average grain size. After grounding and annealing, samples were submitted to 4-point bending strength tests, achieving values of 504 and 540 MPa for 10 mol% and 12 mol% Ce-TZP samples, respectively. Sun et al. [99] fabricated 12 mol % ceria-stabilized zirconia by cold isostatic pressing and sintering at 1450 °C for 3 h, obtaining a microstructure with an average grain size close to 3 μm. The three-point bending strength (n. tested samples = 10, bars of 3 mm thickness, 4 mm width and support span of 60 mm) was $<$ 450 MPa Finally, Turon-Vinas et al. [100] fabricated 10 mol% and 12 mol% ceria-stabilized zirconia by cold isostatic pressing and sintering at 1500 °C for 2 h, obtaining sintered materials with average particle size of around 2 μm and a monoclinic fraction of 78 %. Biaxial flexure strength (ball-on-three-balls testing fixture) was measured on discs (n. tested samples = 5–8, 3.5 mm diameter and ~1.5 mm thick, polished to 3 μm finish) indicated a flexural strength of around 400 and 600 MPa for 10 mol% and 12 mol% Ce-TZP, respectively

In general, the mechanical strength achieved in this study is in line with previous literature on similar materials obtained by 3D printing as well as conventional processing methods, and can be considered more than satisfactory if considered that samples are mechanically characterized as-sintered, meaning without any grinding and machining

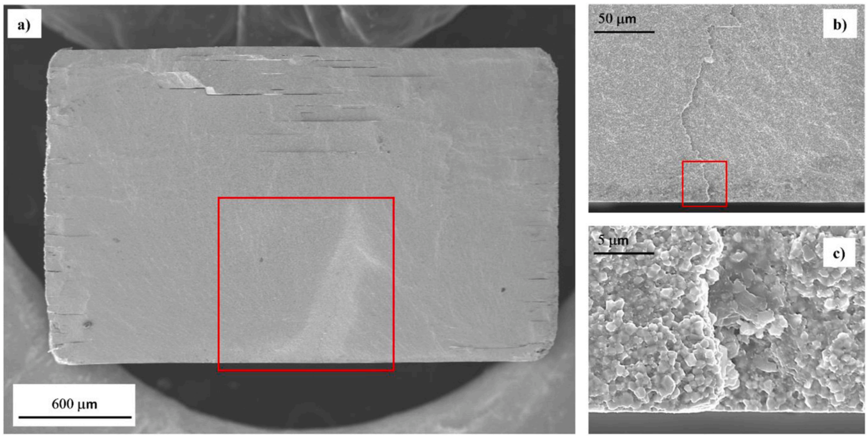

Fig. 12. FESEM micrographs, at different magnifications, carried out on the fracture surface of CEZ-BM-600 sintered at 1350 °C for 0.5 h. a) Full cross-section with highlighted (red square) the possible origin of the crack during 3-point bending test (tensile side); b) and c) details of the defect responsible of the crack origin.

process, contrary to most of the previous literature [97–100].

The knowledge acquired in this work will be transferred to CEZ-based composite materials, with the aim of fabricating 3D printed materials characterized by a combination of exceptional properties, like fracture strength, fracture toughness, reliability and stability, thus to be applied in new mechanical and biomedical applications.

4. Conclusions

This study focuses on the elaboration of ceria-stabilized zirconia ceramics by Digital Light Processing (DLP), with the aim of deepening the role of the ceramic powder features on the different steps involved in the process. Therefore, commercial ceria-stabilized zirconia powders were submitted to mechanical and thermal pre-treatments, to investigate the impact of surface and structural modifications of the powders on the slurry printability, as well as on the sintered density, microstructure and mechanical behaviour.

Three distinct powder batches, namely un-milled, ball-milled, and ball-milled and thermally post-treated were compared. Ball milling effectively reduced the size of micron-scale agglomerates in the un-milled batch, resulting in a loosely dispersed ultrafine powder. However, the mechanical treatment increased the monoclinic zirconia phase content and induced the appearance of oxygen vacancies, likely due to the partial reduction of cerium from its tetravalent to trivalent state. The presence of surface oxygen vacancies, combined with certain ceria segregation on the zirconia surface, led to increased UV absorbance, thereby hindering effective photopolymerization of the slurries. The subsequent calcination step successfully restored the tetravalent oxidation state, reducing the exposure energy required for photopolymerization and enabling the production of nearly defect-free samples.

For the optimized material, a critical aspect of this study was the optimization of the sintering cycle to achieve the best compromise between high sintered density, low monoclinic zirconia content, and a refined microstructure. The optimal sintering conditions were identified as 1350 °C for 0.5 hours, yielding a dense ceramic with a fine microstructure (0.60 ± 0.23 µm) and a low monoclinic phase content (13 vol %), resulting in a remarkably high flexural strength (561 ± 15 MPa).

This work demonstrated the critical importance of optimizing feedstock powder characteristics and comprehensively understanding their role at each stage of the additive manufacturing process. The insights gained from this study will contribute to the development of ceria-stabilized zirconia-based composite materials and the fabrication of complex, targeted components for advanced technological applications.

CRediT authorship contribution statement

Fiume Elisa: Methodology, Investigation, Data curation. **Coppola Bartolomeo:** Writing – review & editing, Methodology, Investigation, Formal analysis, Data curation, Conceptualization. **Montanaro Laura:** Writing – review & editing, Supervision, Resources, Project administration, Methodology, Investigation, Funding acquisition, Conceptualization. **Terranova Vanessa:** Writing – review & editing, Methodology, Investigation, Data curation. **Palmero Paola:** Writing – review & editing, Writing – original draft, Validation, Supervision, Resources, Project administration, Methodology, Investigation, Funding acquisition, Data curation, Conceptualization.

Declaration of Competing Interest

The authors declare that they have no known competing financial interests or personal relationships that could have appeared to influence the work reported in this paper.

Acknowledgements

This work has been supported by the project "CONCERTO – Multiscale modelling/characterization and fabrication of nanocomposite ceramics with improved toughness" funded by the MIUR Progetti di Ricerca di Rilevante Interesse Nazionale (PRIN) Bando 2020 - grant 2020BN5ZW9.

This paper was also partially supported in the frame of the project NODES which has received funding from the MUR – M4C2 1.5 of PNRR funded by the European Union – NextGenerationEU Mission 4 Component 2 - ECS00000036 - CUP E13B22000020001.

References

[1] J.R. Kelly, I. Denry, Stabilized zirconia as a structural ceramic: an overview, Dent. Mater. 24 (3) (2008) 289–298, https://doi.org/10.1016/j.dental.2007.05.005.
[2] P.F. Manicone, P.R. Iommetti, L. Raffaelli, An overview of zirconia ceramics: basic properties and clinical applications, J. Dent. 35 (11) (2007) 819–826, https://doi.org/10.1016/j.jdent.2007.07.008.
[3] C. Piconi, G. Maccauro, Zirconia as a ceramic biomaterial, Biomaterials 20 (1) (1999) 1–25, https://doi.org/10.1016/S0142-9612(98)00010-6.
[4] J. Chevalier, L. Gremillard, Ceramics for medical applications: a picture for the next 20 years, J. Eur. Ceram. Soc. 29 (7) (2009) 1245–1255, https://doi.org/10.1016/j.jeurceramsoc.2008.08.025.
[5] W.O. Soboyejo, J.D. Obayemi, E. Annan, E.K. Ampaw, L. Daniels, N. Rahbar, Review of high temperature ceramics for aerospace applications, Adv. Mater. Res. 1132 (2016) 385–407, https://doi.org/10.4028/www.scientific.net/amr.1132.385.
[6] E. Camposilvan, F.G. Marro, A. Mestra, M. Anglada, Enhanced reliability of yttria-stabilized zirconia for dental applications, Acta Biomater. 17 (2015) 36–46, https://doi.org/10.1016/j.actbio.2015.01.023.
[7] M. Cattani-Lorente, S.S. Scherrer, P. Ammann, M. Jobin, H.A. Wiskott, Low temperature degradation of a Y-TZP dental ceramic, Acta Biomater. 7 (2) (2011) 858–865, https://doi.org/10.1016/j.actbio.2010.09.020.
[8] J. Chevalier, L. Gremillard, S. Deville, Low-temperature degradation of zirconia and implications for biomedical implants, Annu. Rev. Mater. Res. 37 (1) (2007) 1–32, https://doi.org/10.1146/annurev.matsci.37.052506.084250.
[9] K. Tsukuma, M. Shimada, Strength, fracture toughness and Vickers hardness of CeO_2-stabilized tetragonal ZrO_2 polycrystals (Ce-TZP), J. Mater. Sci. 20 (1985) 1178–1184, https://doi.org/10.1007/BF01026311.
[10] H. El Attaoui, M. Saâdaoui, J. Chevalier, G. Fantozzi, Static and cyclic crack propagation in Ce-TZP ceramics with different amounts of transformation toughening, J. Eur. Ceram. Soc. 27 (2-3) (2007) 483–486, https://doi.org/10.1016/j.jeurceramsoc.2006.04.108.
[11] P. Palmero, M. Fornabaio, L. Montanaro, H. Reveron, C. Esnouf, J. Chevalier, Towards long lasting zirconia-based composites for dental implants. Part I: innovative synthesis, microstructural characterization and in vitro stability, Biomaterials 50 (2015) 38–46, https://doi.org/10.1016/j.biomaterials.2015.01.018.
[12] H. Reveron, M. Fornabaio, P. Palmero, T. Fürderer, E. Adolfsson, V. Lughi, A. Bonifacio, V. Sergo, L. Montanaro, J. Chevalier, Towards long lasting zirconia-based composites for dental implants: transformation induced plasticity and its consequence on ceramic reliability, Acta Biomater. 48 (2017) 423–432, https://doi.org/10.1016/j.actbio.2016.11.040.
[13] B. Altmann, L. Karygianni, A. Al-Ahmad, F. Butz, M. Bächle, E. Adolfsson, T. Fürderer, N. Curtois, P. Palmero, M. Follo, J. Chevalier, T. Steinberg, R. J. Kohal, Assessment of novel long-lasting ceria-stabilized zirconia-based ceramics with different surface topographies as implant materials, Adv. Funct. Mater. 27 (40) (2017) 1702512, https://doi.org/10.1002/adfm.201702512.
[14] B. Altmann, K. Rabel, R.J. Kohal, S. Proksch, P. Tomakidi, E. Adolfsson, F. Bernsmann, P. Palmero, T. Fürderer, T. Steinberg, Cellular transcriptional response to zirconia-based implant materials, Dent. Mater. 33 (2) (2017) 241–255, https://doi.org/10.1016/j.dental.2016.12.005.
[15] M. Li, S. Cokic, B. Van Meerbeek, J. Vleugels, F. Zhang, Novel zirconia ceramics for dental implant materials, J. Mater. Sci. Technol. 210 (2025) 97–108, https://doi.org/10.1016/j.jmst.2024.05.041.
[16] Y. Hagiwara, K. Nakajima, Use of ceria-stabilized zirconia/alumina nanocomposite for fabricating the frameworks of removable dental prostheses: a clinical report, J. Prosthet. Dent. 116 (2) (2016) 166–171, https://doi.org/10.1016/j.prosdent.2016.01.020.
[17] Y. Tian, Y. Song, S. Lan, R. Geng, M. Wang, S. Li, J. Han, H. Bai, G. Hong, Y. Li, Ceria-stabilized zirconia/alumina nanocomposite (NANO-Zr) surface enhances osteogenesis through regulation of macrophage polarization, Coatings 14 (11) (2024) 1460, https://doi.org/10.3390/coatings14111460.
[18] R. Martin, M. Vick, R.K. Enneti, S.V. Atre, Powder injection molding of ceria-stabilized, zirconia-toughened mullite parts for UAV engine components, JOM 65 (2013) 1388–1394, https://doi.org/10.1007/s11837-013-0673-5.
[19] Z. Chen, Z. Li, J. Li, C. Liu, C. Lao, Y. Fu, C. Liu, Y. Li, P. Wang, Y. He, 3D printing of ceramics: a review, J. Eur. Ceram. Soc. 39 (4) (2019) 661–687, https://doi.org/10.1016/j.jeurceramsoc.2018.11.013.

[20] S. Zakeri, M. Vippola, E. Levänen, A comprehensive review of the photopolymerization of ceramic resins used in stereolithography, Addit. Manuf. 35 (2020) 101177, https://doi.org/10.1016/j.addma.2020.101177.

[21] K. Kendall, Influence of powder structure on processing and properties of advanced ceramics, Powder Technol. 58 (3) (1989) 151–161, https://doi.org/10.1016/0032-5910(89)80109-3.

[22] R. Moreno, Better ceramics through colloid chemistry, J. Eur. Ceram. Soc. 40 (3) (2020) 559–587, https://doi.org/10.1016/j.jeurceramsoc.2019.10.014.

[23] J.A. Mangels, The role of powder properties in ceramic processing, in: Proceedings of the Thirteenth Automotive Materials Conference, in: Ceramic Engineering and Science Proceedings, 7, John Wiley & Sons, Inc, Hoboken, NJ, USA, 1986, pp. 1112–1121, https://doi.org/10.1002/9780470320358.ch3.

[24] A. Bove, F. Calignano, M. Galati, L. Iuliano, Photopolymerization of ceramic resins by stereolithography process: a review, Appl. Sci. 12 (7) (2022) 3591, https://doi.org/10.3390/app12073591.

[25] X. Xu, S. Zhou, J. Wu, S. Liu, S. Ma, T. Cheng, Study of alumina ceramic parts fabricated via DLP stereolithography using powders with different sizes and morphologies, Int. J. Appl. Ceram. Technol. 20 (2) (2023) 1167–1193, https://doi.org/10.1111/ijac.14245.

[26] H. Yang, T. He, Q. Lv, Y. San, X. Xu, J. Xiong, J. Liu, Effects of powder morphology on stereolithography additive manufactured Al_2O_3 ceramic, J. Mater. Res. Technol. 29 (2024) 504–510, https://doi.org/10.1016/j.jmrt.2024.01.075.

[27] H. Wu, Y. Cheng, W. Liu, R. He, M. Zhou, S. Wu, X. Song, Y. Chen, Effect of the particle size and the debinding process on the density of alumina ceramics fabricated by 3D printing based on stereolithography, Ceram. Int. 42 (15) (2016) 17290–17294, https://doi.org/10.1016/j.ceramint.2016.08.024.

[28] C. Qian, K. Hu, H. Wang, L. Nie, Q. Feng, Z. Lu, Li Peijie, K. Lu, The effect of particle size distribution on the microstructure and properties of Al_2O_3 ceramics formed by stereolithography, Ceram. Int. 48 (15) (2022) 21600–21609, https://doi.org/10.1016/j.ceramint.2022.04.133.

[29] X. Xu, J. Qiu, Z. Li, Y. Liu, Y. Wu, Particle grading and debinding process of zirconia ceramic based on digital light process, Ceram. Int. 50 (21) (2024) 43424–43432, https://doi.org/10.1016/j.ceramint.2024.08.193.

[30] L. Fan, C. Huang, H. Liu, Z. Wang, L. Xu, S. Huang, M. Qu, Z. Xu, S. Li, S. Xu, The effect of ZrO_2 particle size and solid loading on the rheological properties of highly thixotropic ZrO_2 ceramic slurries applied in photopolymerization 3D printing, Ceram. Int. (2024), https://doi.org/10.1016/j.ceramint.2024.12.111.

[31] H. Xing, B. Zou, X. Liu, X. Wang, Q. Chen, X. Fu, Y. Li, Effect of particle size distribution on the preparation of ZTA ceramic paste applying for stereolithography 3D printing, Powder Technol. 359 (2020) 314–322, https://doi.org/10.1016/j.powtec.2019.09.066.

[32] M. Liu, Y. Wang, H. Zhang, Q. Wei, Z. Liu, X. Liu, Influence of particle size distribution on hydroxyapatite slurry and scaffold properties fabricated using digital light processing, J. Manuf. Process. 131 (2024) 401–411, https://doi.org/10.1016/j.jmapro.2024.09.036.

[33] E.K. Goharshadi, S. Samiee, P. Nancarrow, Fabrication of cerium oxide nanoparticles: characterization and optical properties, J. Colloid Interface Sci. 356 (2) (2011) 473–480, https://doi.org/10.1016/j.jcis.2011.01.063.

[34] K. Tsukuma, M. Shimada, Strength, fracture toughness and Vickers hardness of CeO_2-stabilized tetragonal ZrO_2 polycrystals (Ce-TZP), J. Mater. Sci. 20 (1985) 1178–1184, https://doi.org/10.1007/BF01026311.

[35] S. Fournier, J. Chevalier, G.P. Baeza, C. Chaput, E. Louradour, P. Sainsot, J. Cavoret, H. Reveron, Ceria-stabilized zirconia-based composites printed by stereolithography: impact of the processing method on the ductile behaviour and its transformation features, J. Eur. Ceram. Soc. 43 (7) (2023) 2894–2906, https://doi.org/10.1016/j.jeurceramsoc.2022.11.006.

[36] B. Inserra, B. Coppola, L. Montanaro, J.M. Tulliani, P. Palmero, Preparation and characterization of Ce-ZrO_2/Al_2O_3 composites by DLP-based stereolithography, J. Eur. Ceram. Soc. 43 (7) (2023) 2907–2916, https://doi.org/10.1016/j.jeurceramsoc.2022.08.037.

[37] Daiichi Kigenso Kagaku Kogyo Co., Ltd, Osaka, Japan. (Accessed January 2025). ⟨http://www.dkkk.co.jp/english⟩.

[38] M. Pradhan, P.C. Kapur, Effect of powder dispersion on sintering behavior and mechanical properties of nanostructured 3YSZ ceramics, Ceram. Int. 38 (4) (2012) 2835–2843, https://doi.org/10.1016/j.ceramint.2011.11.055.

[39] J. Adam, R. Drumm, G. Klein, M. Veith, Milling of zirconia nanoparticles in a stirred media mill, J. Am. Ceram. Soc. 91 (9) (2008) 2836–2843, https://doi.org/10.1111/j.1551-2916.2008.02579.x.

[40] Z.R. Hesabi, A. Simchi, S.S. Reihani, Structural evolution during mechanical milling of nanometric and micrometric Al_2O_3 reinforced Al matrix composites, Mater. Sci. Eng. A 428 (1-2) (2006) 159–168, https://doi.org/10.1016/j.msea.2006.04.116.

[41] F. Delogu, G. Cocco, Microstructural refinement of ceramic powders under mechanical processing conditions, J. Alloy. Compd. 420 (1-2) (2006) 246–250, https://doi.org/10.1016/j.jallcom.2005.10.037.

[42] H. Toraya, M. Yoshimura, S. Somiya, Calibration curve for quantitative analysis of the monoclinic-tetragonal ZrO_2 system by X-ray diffraction, J. Am. Ceram. Soc. 67 (6) (1984) C-119, https://doi.org/10.1111/j.1151-2916.1984.tb19715.x.

[43] M. Mohammadi, B. Coppola, L. Montanaro, P. Palmero, Digital light processing of high-strength hydroxyapatite ceramics: role of particle size and printing parameters on microstructural defects and mechanical properties, J. Eur. Ceram. Soc. 43 (7) (2023) 2761–2772, https://doi.org/10.1016/j.jeurceramsoc.2022.11.047.

[44] N. Li, F. Zhai, Z. Yi, L. Gao, Z. Xie, Y. He, Y. Jiang, Sintering kinetics of cerium-stabilised tetragonal zirconia, Ceram. Int. 50 (1) (2024) 1581–1590, https://doi.org/10.1016/j.ceramint.2023.10.250.

[45] M. Lakusta, I. Danilenko, G. Volkova, L. Loladze, G. Golovan, I. Brukhanova, V. Glazunova, I. Popov, O. Mazur, T. Konstantinova, Effect of mechanical activation on sintering behaviour of tetragonal zirconia nanopowders, Ceram. Int. 46 (9) (2020) 13953–13960, https://doi.org/10.1016/j.ceramint.2020.02.193.

[46] M. Skovgaard, A. Ahniyaz, B.F. Sørensen, K. Almdal, A. Van Lelieveld, Effect of microscale shear stresses on the martensitic phase transformation of nanocrystalline tetragonal zirconia powders, J. Eur. Ceram. Soc. 30 (13) (2010) 2749–2755, https://doi.org/10.1016/j.jeurceramsoc.2010.05.025.

[47] J.D. Lin, J.G. Duh, The use of X-ray line profile analysis in the tetragonal to monoclinic phase transformation of ball milled, as-sintered and thermally aged zirconia powders, J. Mater. Sci. 32 (1997) 4901–4908, https://doi.org/10.1023/A:1018668006162.

[48] Fornabaio, M. Composites in the Alumina-Zirconia System: an Engineering Approach for an Effective Tailoring of Microstructural Features and Performances (Ph.D. thesis), Politecnico di Torino and Institut National des Sciences Appliquées de Lyon, 2014. ⟨https://hdl.handle.net/11583/2553736⟩.

[49] J. Judes, V. Kamaraj, Sol–gel preparation and characterization of ceria stabilized zirconia minispheres, J. Sol. Gel Sci. Technol. 49 (2009) 159–165, https://doi.org/10.1007/s10971-008-1853-6.

[50] R.P. Chhabra, J.F. Richardson, Non-Newtonian fluid behaviour, in: Non-Newtonian Flow and Applied Rheology (2008) 1–55, https://doi.org/10.1016/b978-0-7506-8532-0.00001-9.

[51] S. Fournier, J. Chevalier, H. Reveron, W. Chèvremont, G.P. Baeza, Rheology and structure of ceramic stereolithography slurries: role of powder nature, dispersant, and orthogonal strain, J. Am. Ceram. Soc. 108 (4) (2025) e20304, https://doi.org/10.1111/jace.20304.

[52] O. Peña-Rodríguez, C.F. Sánchez-Valdés, M. Garriga, M.I. Alonso, X. Obradors, T. Puig, Optical properties of ceria–zirconia epitaxial films grown from chemical solutions, Mater. Chem. Phys. 138 (2-3) (2013) 462–467, https://doi.org/10.1016/j.matchemphys.2012.11.069.

[53] C. Qian, K. Hu, J. Li, P. Li, Z. Lu, The effect of light scattering in stereolithography ceramic manufacturing, J. Eur. Ceram. Soc. 41 (14) (2021) 7141–7154, https://doi.org/10.1016/j.jeurceramsoc.2021.07.017.

[54] N. Kovacev, S. Li, K. Essa, Effect of the preparation techniques of photopolymerizable ceramic slurry and printing parameters on the accuracy of 3D printed lattice structures, J. Eur. Ceram. Soc. 41 (15) (2021) 7734–7743, https://doi.org/10.1016/j.jeurceramsoc.2021.08.052.

[55] J. Sun, J. Binner, J. Bai, 3D printing of zirconia via digital light processing: optimization of slurry and debinding process, J. Eur. Ceram. Soc. 40 (15) (2020) 5837–5844, https://doi.org/10.1016/j.jeurceramsoc.2020.05.079.

[56] G. Mitteramskogler, R. Gmeiner, R. Felzmann, S. Gruber, C. Hofstetter, J. Stampfl, J. Ebert, W. Wachter, J. Laubersheimer, Light curing strategies for lithography-based additive manufacturing of customized ceramics, Addit. Manuf. 1 (2014) 110–118, https://doi.org/10.1016/j.addma.2014.08.003.

[57] Y. Yun, X. Deqiao, J. Chen, D. Zhaoling, S. Lida, T. Zongjun, C. Yunfei, H. Feng, Mechanism of ceramic slurry light scattering affecting contour accuracy and method of projection plane correction, Ceram. Int. 49 (10) (2023) 15024–15033, https://doi.org/10.1016/j.ceramint.2023.01.085.

[58] R.S. Das, S.K. Warkhade, A. Kumar, A.V. Wankhade, Graphene oxide-based zirconium oxide nanocomposite for enhanced visible light-driven photocatalytic activity, Res. Chem. Intermed. 45 (2019) 1689–1705, https://doi.org/10.1007/s11164-018-3699-z.

[59] I. Das, S. Chattopadhyay, A. Mahato, B. Kundu, G. De, Fabrication of a cubic zirconia nanocoating on a titanium dental implant with excellent adhesion, hardness and biocompatibility, RSC Adv. 6 (64) (2016) 59030–59038, https://doi.org/10.1039/C6RA10661G.

[60] M. Hajizadeh-Oghaz, R. Shoja Razavi, A. Ghasemi, Synthesis and characterization of ceria–yttria co-stabilized zirconia (CYSZ) nanoparticles by sol–gel process for thermal barrier coatings (TBCs) applications, J. Sol. Gel Sci. Technol. 74 (3) (2015) 603–612, https://doi.org/10.1007/s10971-015-3639-y.

[61] V. Gayathri, R. Balan, Synthesis and characterisation of pure zirconium Oxide (ZrO_2) nanoparticle by conventional precipitation method, J. Environ. Nanotechnol. 10 (2021) 12–14, https://doi.org/10.13074/jent.2021.12.214447.

[62] R. Pitcheri, S.P. Mooni, D. Radhalayam, M. Nora, S. Roy, F.A.M. Al-Zahrani, M. Suneetha, Effect of Ce-doping on the structural, morphological, and electrochemical features of Co_3O_4 nanoparticles synthesized by solution combustion method for battery-type supercapacitors, Ceram. Int. 50 (23) (2024) 50504–50515, https://doi.org/10.1016/j.ceramint.2024.09.396.

[63] M.I. Zaki, M.A. Hasan, L. Pasupulety, Surface reactions of acetone on Al_2O_3, TiO_2, ZrO_2, and CeO_2: IR spectroscopic assessment of impacts of the surface acid−base properties, Langmuir 17 (3) (2001) 768–774, https://doi.org/10.1021/la000976p.

[64] A. Galtayries, R. Sporken, J. Riga, G. Blanchard, R. Caudano, XPS comparative study of ceria/zirconia mixed oxides: powders and thin film characterisation, J. Electron Spectrosc. Relat. Phenom. 88 (1998) 951–956, https://doi.org/10.1016/S0368-2048(97)00134-5.

[65] F. Jonas, B. Lebeau, S. Siffert, L. Michelin, C. Poupin, R. Cousin, L. Josien, L. Vidal, M. Mallet, P. Gaudin, J.L. Blin, Nanoporous CeO_2–ZrO_2 oxides for oxidation of volatile organic compounds, ACS Appl. Nano Mater. 4 (2) (2021) 1786–1797, https://doi.org/10.1021/acsanm.0c03212.

[66] P.M. Shah, J.W. Burnett, D.J. Morgan, T.E. Davies, S.H. Taylor, Ceria–zirconia mixed metal oxides prepared via mechanochemical grinding of carbonates for the total oxidation of propane and naphthalene, Catalysts 9 (5) (2019) 475, https://doi.org/10.3390/catal9050475.

[67] I.N. Demchenko, K. Nikiforow, M. Chernyshova, Y. Melikhov, Y. Syryanyy, N. Korsunska, L. Khomenkova, Y. Brodnikovskyi, D. Brodnikovskyi, X-ray

photoelectron spectroscopy analysis of scandia-ceria-stabilized zirconia composites with different transport properties, Materials 16 (16) (2023) 5504, https://doi.org/10.3390/ma16165504.

[68] G. Issa, M. Kormunda, O. Tumurbaatar, Á. Szegedi, D. Kovacheva, D. Karashanova, M. Popova, Impact of Ce/Zr ratio in the nanostructured ceria and zirconia composites on the selective CO_2 adsorption, Nanomaterials 13 (17) (2023) 2428, https://doi.org/10.3390/nano13172428.

[69] S.R. Teeparthi, E.W. Awin, R. Kumar, Dominating role of crystal structure over defect chemistry in black and white zirconia on visible light photocatalytic activity, Sci. Rep. 8 (1) (2018) 5541, https://doi.org/10.1038/s41598-018-23648-0.

[70] M.A. Gondal, T.A. Fasasi, U. Baig, A. Mekki, Effects of oxidizing media on the composition, morphology and optical properties of colloidal zirconium oxide nanoparticles synthesized via pulsed laser ablation in liquid technique, J. Nanosci. Nanotechnol. 18 (6) (2018) 4030–4039, https://doi.org/10.1166/jnn.2018.15244.

[71] I. Bespalov, M. Datler, S. Buhr, W. Drachsel, G. Rupprechter, Y. Suchorski, Initial stages of oxide formation on the Zr surface at low oxygen pressure: an in situ FIM and XPS study, Ultramicroscopy 159 (2015) 147–151, https://doi.org/10.1016/j.ultramic.2015.02.016.

[72] C.O. De González, E.A. García, An X-ray photoelectron spectroscopy study of the surface oxidation of zirconium, Surf. Sci. 193 (3) (1988) 305–320, https://doi.org/10.1016/0039-6028(88)90438-4.

[73] A. Sinhamahapatra, J.P. Jeon, J. Kang, B. Han, J.S. Yu, Oxygen-deficient zirconia (ZrO_{2-x}): a new material for solar light absorption, Sci. Rep. 6 (1) (2016) 27218, https://doi.org/10.1038/srep27218.

[74] B. Dashtbozorg, F. Shi, A. Tagliaferro, S. Abela, L. Falticeanu, H. Dong, Plasma defect-engineering of bulk oxygen-deficient zirconia, Acta Mater. 262 (2024) 119457, https://doi.org/10.1016/j.actamat.2023.1194.

[75] T.S. Wu, L.Y. Syu, C.N. Lin, B.H. Lin, Y.H. Liao, S.C. Weng, Y.J. Huang, H.T. Jeng, S.Y. Lu, S.L. Chang, Y.L. Soo, Enhancement of catalytic activity by UV-light irradiation in CeO_2 nanocrystals, Sci. Rep. 9 (1) (2019) 8018, https://doi.org/10.1038/s41598-019-44543-2.

[76] Rinaudo, M.G., Cadús, L.E., Morales, M.R. (2023). Mechanochemical activation of CeO_2 in order to boost physicochemical properties for catalytic applications, Eng. Proc., 56(1), 49. ⟨https://doi.org/10.3390/ASEC2023-15402⟩.

[77] R. Ma, M.J. Islam, D.A. Reddy, T.K. Kim, Transformation of CeO_2 into a mixed phase CeO_2/Ce_2O_3 nanohybrid by liquid phase pulsed laser ablation for enhanced photocatalytic activity through Z-scheme pattern, Ceram. Int. 42 (16) (2016) 18495–18502, https://doi.org/10.1016/j.ceramint.2016.08.186.

[78] A. Trovarelli, F. Zamar, J. Llorca, C. De Leitenburg, G. Dolcetti, J.T. Kiss, Nanophase fluorite-structured CeO_2–ZrO_2 Catalysts prepared by high-energy mechanical milling, J. Catal. 169 (2) (1997) 490–502, https://doi.org/10.1006/jcat.1997.1705.

[79] P. Janoš, T. Hladík, M. Kormunda, J. Ederer, M. Šťastný, Thermal treatment of cerium oxide and its properties: adsorption ability versus degradation efficiency, Adv. Mater. Sci. Eng. 2014 (1) (2014) 706041, https://doi.org/10.1155/2014/706041.

[80] T. Arii, T. Taguchi, A. Kishi, M. Ogawa, Y. Sawada, Thermal decomposition of cerium (III) acetate studied with sample-controlled thermogravimetric–mass spectrometry (SCTG—MS), J. Eur. Ceram. Soc. 22 (13) (2002) 2283–2289, https://doi.org/10.1016/S0955-2219(02)00019-5.

[81] R. Grau-Crespo, N.H. de Leeuw, S. Hamad, U.V. Waghmare, Phase separation and surface segregation in ceria–zirconia solid solutions, Proc. R. Soc. A Math., Phys. Eng. Sci. 467 (2131) (2011) 1925–1938, https://doi.org/10.1098/rspa.2010.0512.

[82] S. Damyanova, B. Pawelec, K. Arishtirova, M.M. Huerta, J.L.G. Fierro, Study of the surface and redox properties of ceria–zirconia oxides, Appl. Catal. A Gen. 337 (1) (2008) 86–96, https://doi.org/10.1016/j.apcata.2007.12.005.

[83] D. Panayotov, V. Zdravkova, O. Lagunov, S. Andonova, I. Spassova, D. Nihtianova, G. Atanasova, N. Drenchev, E. Ivanova, M. Mihaylov, K. Hadjiivanov, Capturing CO_2 by ceria and ceria–zirconia nanomaterials of different origin, Phys. Chem. Chem. Phys. 25 (26) (2023) 17154–17175, https://doi.org/10.1039/d3cp00896g.

[84] H. Idriss, On the wrong assignment of the XPS O1s signal at 531–532 eV attributed to oxygen vacancies in photo-and electro-catalysts for water splitting and other materials applications, Surf. Sci. 712 (2021) 121894, https://doi.org/10.1016/j.susc.2021.121894.

[85] J. Wu, Z. Zhao, C.M. Hamel, X. Mu, X. Kuang, Z. Guo, H.J. Qi, Evolution of material properties during free radical photopolymerization, J. Mech. Phys. Solids 112 (2018) 25–49, https://doi.org/10.1016/j.jmps.2017.11.018.

[86] Q. Zhang, S. Weng, C.M. Hamel, S.M. Montgomery, J. Wu, X. Kuang, K. Zhou, H. J. Qi, Design for the reduction of volume shrinkage-induced distortion in digital light processing 3D printing, Extrem. Mech. Lett. 48 (2021) 101403, https://doi.org/10.1016/j.eml.2021.101403.

[87] D. Wu, Z. Zhao, Q. Zhang, H.J. Qi, D. Fang, Mechanics of shape distortion of DLP 3D printed structures during UV post-curing, Soft Matter 15 (30) (2019) 6151–6159, https://doi.org/10.1039/c9sm00725c.

[88] P. Dolez, M. Marek, B.J. Love, Photopolymerizable acrylic resin: effect of curing time and temperature, J. Appl. Polym. Sci. 82 (3) (2001) 546–554, https://doi.org/10.1002/app.1881.

[89] K. Trembecka-Wójciga, J. Ortyl, Enhancing 3D printed ceramic components: the function of dispersants, adhesion promoters, and surface-active agents in photopolymerization-based additive manufacturing, Adv. Colloid Interface Sci. (2024) 103251, https://doi.org/10.1016/j.cis.2024.103251.

[90] K.R. Kambale, A. Mahajan, S.P. Butee, Effect of grain size on the properties of ceramics, Met. Powder Rep. 74 (3) (2019) 130–136, https://doi.org/10.1016/j.mprp.2019.04.060.

[91] S.B. Kim, D.Y. Kim, J.J. Kim, S.H. Cho, Effect of grain size and poling on the fracture mode of lead zirconate titanate ceramics, J. Am. Ceram. Soc. 73 (1) (1990) 161–163, https://doi.org/10.1111/j.1151-2916.1990.tb05113.x.

[92] C.M. Ramos, P.F. Cesar, E.A. Bonfante, J.H. Rubo, L. Wang, A.F.S. Borges, Fractographic principles applied to Y-TZP mechanical behavior analysis, J. Mech. Behav. Biomed. Mater. 57 (2016) 215–223, https://doi.org/10.1016/j.jmbbm.2015.12.006.

[93] S.S. Scherrer, U. Lohbauer, A. Della Bona, A. Vichi, M.J. Tholey, J.R. Kelly, R. van Noort, P.F. Cesar, ADM guidance—ceramics: guidance to the use of fractography in failure analysis of brittle materials, Dent. Mater. 33 (6) (2017) 599–620, https://doi.org/10.1016/j.dental.2017.03.004.

[94] M. Inokoshi, H. Liu, K. Yoshihara, M. Yamamoto, W. Tonprasong, Y. Benino, S. Minakuchi, J. Vleugels, B. Van Meerbeek, F. Zhang, Layer characteristics in strength-gradient multilayered yttria-stabilized zirconia, Dent. Mater. 39 (4) (2023) 430–441, https://doi.org/10.1016/j.dental.2023.03.015.

[95] Z. Li, J. Wu, J. Luo, B. Zhang, Y. Li, B. Cheng, J. Yang, B. Li, X. Wang, Effects of alumina modification on curing performance of ceria-stabilized zirconia in stereolithography, J. Alloy. Compd. 1012 (2025) 178438, https://doi.org/10.1016/j.jallcom.2024.178438.

[96] R. Zhao, X. Liu, H. Li, L. Song, J. Ma, Stronger and tougher nanosized dense ceria-doped tetragonal zirconia polycrystals by sinter-HIP, J. Eur. Ceram. Soc. 43 (5) (2023) 2282–2288, https://doi.org/10.1016/j.jeurceramsoc.2022.12.046.

[97] S.C. Sharma, N.M. Gokhale, R. Dayal, R. Lal, Synthesis, microstructure and mechanical properties of ceria stabilized tetragonal zirconia prepared by spray drying technique, Bull. Mater. Sci. 25 (2002) 15–20, https://doi.org/10.1007/BF02704588.

[98] H. El Attaoui, M. Saâdaoui, J. Chevalier, G. Fantozzi, Static and cyclic crack propagation in Ce-TZP ceramics with different amounts of transformation toughening, J. Eur. Ceram. Soc. 27 (2-3) (2007) 483–486, https://doi.org/10.1016/j.jeurceramsoc.2006.04.108.

[99] Z. Sun, X. Li, J. Xing, M. Gan, Z. Ji, Y. Lyu, Improving the mechanical properties and microstructure of 12 mol% Ceria-stabilized tetragonal zirconia polycrystal ceramics with low-content Nd2O3, Materials 17 (22) (2024) 5426, https://doi.org/10.3390/ma17225426.

[100] M. Turon-Vinas, F. Zhang, J. Vleugels, M. Anglada, Effect of calcia co-doping on ceria-stabilized zirconia, J. Eur. Ceram. Soc. 38 (6) (2018) 2621–2631, https://doi.org/10.1016/j.jeurceramsoc.2017.12.053.